S.G. Robson, P. Räcke, A.M. Jakob, N. Collins, H.R. Firgau, V. Schmitt, V. Mourik, A. Morello, E. Mayes, D. Spemann, and D.N. Jamieson

Near-Surface Electrical Characterisation of Silicon Electronic Devices Using Focused keV Ions

S. G. Robson,[1, *] P. Räcke,[2, 3] A. M. Jakob,[1] N. Collins,[1] H. R. Firgau,[4] V. Schmitt,[4]
V. Mourik,[4] A. Morello,[4] E. Mayes,[5] D. Spemann,[2, 3] and D. N. Jamieson[1]

[1]*Centre for Quantum Computation and Communication Technology,*
School of Physics, University of Melbourne, Parkville VIC 3010, Australia
[2]*Leibniz Institute of Surface Engineering (IOM), Permoserstr. 15, D-04318 Leipzig, Germany*
[3]*Leibniz Joint Lab 'Single Ion Implantation', Permoserstr. 15, D-04318 Leipzig, Germany*
[4]*Centre for Quantum Computation and Communication Technology,*
School of Electrical Engineering and Telecommunications, UNSW Sydney, Sydney NSW 2052, Australia
[5]*RMIT Microscopy and Microanalysis Facility, RMIT University, Melbourne VIC 3001, Australia*
(Dated: August 15, 2022)

The demonstration of universal quantum logic operations near the fault-tolerance threshold has established ion-implanted near-surface donor atoms as a plausible platform for scalable quantum computing in silicon. The next technological step forward requires a deterministic fabrication method to create large-scale arrays of donors, featuring few hundred nanometre inter-donor spacing. Here, we explore the feasibility of this approach by implanting low-energy ions into silicon devices featuring a $60 \times 60 \, \mu m^2$ sensitive area and an ultra-thin 3.2 nm gate oxide – capable of hosting large-scale donor arrays. We employ a characterisation system consisting of a modified focused ion beam machine and ultra-low noise ion detection electronics to demonstrate a method for evaluating the device response characteristics to shallowly implanted 12 keV $^1H_2^+$ ions. Despite the weak internal electric field, near-unity charge collection efficiency is obtained from the entire sensitive area. This can be explained by the critical role that the thermal gate oxide plays in the ion detection response, allowing an initial rapid diffusion of ion induced charge away from the implant site. Next, we adapt our approach to perform deterministic implantation of a few thousand 24 keV $^{40}Ar^{2+}$ ions into a predefined micro-volume, without any additional collimation. Despite the reduced ionisation from the heavier ion species, a fluence-independent detection confidence of $\geq 99.99\%$ was obtained. Our system thus represents not only a method for mapping the near-surface electrical landscape of electronic devices, but also a framework towards mask-free prototyping of large-scale donor arrays in silicon.

I. INTRODUCTION

Devices based on complementary metal–oxide semiconductor (CMOS) technology, both in established applications for classical information technology and in emerging applications for quantum computing, depend on the precise control of electric fields in the near-surface region. In classical silicon transistors, the source-drain current flowing beneath a thin (<10 nm) gate oxide is modulated by the electric field from a surface gate [1]. The current flows in thin sheets, with the highest density closest to the Si-SiO$_2$ interface [2]. With the transistor size inside modern processors now approaching 5 nm [3], the concentration of fabrication defects on the nanoscale has become a critical issue. For example, local oxide thickness fluctuations, trapped interface charge, and atomic-scale interface roughness can strongly affect the device internal electric field, leading to device reliability issues and breakdown [4, 5]. In devices engineered for quantum applications, the electronic and nuclear spin of near-surface (<20 nm deep) donors in silicon can be used to encode information [6]. Each atom's quantum state is programmed and read-out by electric fields from surface gates isolated from the substrate by a thin gate oxide [7]. Small-scale prototype devices have so far demonstrated nuclear coherence times exceeding 30 s [8], gate fidelities beyond 99.9% [9], and more recently, universal quantum logic operations in a three-qubit

processor with >99% fidelity [10]. To satisfy surface code error correction specifications, future quantum devices will require a large number ($>10^6$) of donors arranged in a near-surface array [7]. Besides being an enormous fabrication challenge in its own right, careful control of the internal electric field profile is critical for these devices to correctly function.

Among the possible fabrication pathways to incorporate near-surface donors in silicon, scanning probe lithography can be used to produce few-donor clusters [11] with sub-nm placement precision [12]. An alternative placement approach involves using low-energy ion implantation to produce well-separated individual donors. Already the industry standard for fabricating classical CMOS devices [13], we recently extended this technique with the development of a deterministic ion implantation system that uses the internal electric field within a silicon device to register stochastic arrival-time single ion implantation events [14]. The system was used to demonstrate post-implant counted detection of a few thousand 14 keV P$^+$ ions in Si with 99.85% confidence, using an ion beam collimated to $\sim 10 \, \mu m$ diameter by an in-situ microstencil [14]. The inherent uncertainty of each ion's final resting position in the silicon lattice furthermore meets the relaxed placement constraints of the "flip-flop" qubit architecture [7], where $100 - 500$ nm inter-donor spacing is permitted.

In this work, we investigate the possibility of enhancing this fabrication method to produce large-area arrays of single donors spanning tens of μm – a key prerequisite for a large-scale silicon quantum processor. The analysis is performed within an electronic device characterisation system based on focused ion beam (FIB), a well-understood analysis and fab-

rication technique that has been used within materials science for decades [15]. Typically incorporating a Ga liquid-metal ion source with a $\sim$5 nm beam spot size, FIB can be used for milling microstructures in a variety of materials [16]. More recently, the use of light ion sources such as He and Ne has reduced the beam spot size to <0.5 nm [17], leading to applications in photonics [18] and quantum materials [19]. Using an updated generation of single ion detectors that feature an ultra-thin passivation gate oxide plus an enlarged sensitive area suitable for spin readout and control of donor arrays [7, 14], we first scan a focussed probe of 12 keV $^1H_2^+$ ions across the surface and measure the device's response as a function of beam position. This technique is commonplace for electrical device characterisation at few-µm depths using high-energy MeV ions [20], but here we demonstrate its use in the low keV regime. As such, this provides a method to evaluate the near-surface (<100 nm) electronic properties. For devices that meet appropriate quality acceptance criteria, we then reconfigure the system to perform counted 24 keV $^{40}Ar^{2+}$ implants into the centre of the sensitive region, without the use of an additional mask, and calculate the ion detection confidence. This additionally allows us to assess the future suitability of employing the system to construct donor arrays in silicon.

II. METHODS

A. The Modified FIB System

Experiments took place using a commercially available FIB machine (Raith ionLINE) that has been modified for this work (schematic shown in Fig 1(a)). Full details of the machine are available in [21]. Briefly, the conventional liquid metal ion source was replaced with an electron-beam-ion-source (EBIS) from DREEBIT GmbH [22]. This is a versatile high-brightness gas plasma source that can produce ions in multiple charge states $q = \{1, 2, ...\}$ up to complete ionisation [23]. In this study, Ar^{q+} and H_2^+ molecule ions were employed. The base pressure in the ion source chamber was kept below 10^{-9} mbar. The source potential can vary between $3 - 20$ kV, but was generally set to 12 kV for the these experiments, resulting in a kinetic ion implantation energy of $E = q \times 12$ keV. Mass and charge-state selection occur via an integrated Wien filter, with a retractable Faraday cup located at the source output for ion beam diagnostics. Ion focusing optics comprise of objective and condenser apertures ranging from $1 - 200$ µm in size, selectable via an electrically-driven aperture stage. An octupole stigmator ensures a circular ion beam profile. The beam is de-magnified by the FIB lens system, and can be scanned across the sample stage using the integrated high-speed pattern generator. The working distance is 10 mm. Additionally, the interferometrically controlled sample stage can be positioned to <2 nm accuracy across its entire 200 mm travel range and provides an alternative precision sample stepping method. Coarse lateral ion beam alignment ($\sim$10 µm) is accomplished by an optical camera, and secondary electron imaging via an integrated Everhart-Thornley detector enables precision sample alignment to within $\sim$20 nm. Beam currents between $0.1 - 100$ ion/s are achieved by combining direct filament current control and Wien filter detuning.

B. Single Ion Detection

The ion beam is focused onto a custom-fabricated silicon diode (referred hereafter as a detector) mounted on an integrated preamplifier printed circuit board. The assembly is housed within a metal case (see Fig. 1(b)) which is fixed to the FIB sample stage. The detector design incorporates a localised p-doped top electrode region and a uniform n-doped back contact in 520 µm-thick uniform high purity [001] float zone Si (n-type, 9250 Ω cm) to form a vertical "sandwich type" p–i–n structure, as shown in Fig. 1(c)-(f). The electrodes are metallised with 200 nm-thick Al to form Ohmic contacts for wire bonding. Ions are designed to be implanted into the centre of the detector (region A, referred hereafter as the "construction site", CS), which is covered by a thermally grown passivation gate oxide of between $3 - 6$ nm nominal thickness. The remainder of the detector surface is covered by a thermally grown field oxide of $\sim$65 nm thickness (regions C, D, E in Fig. 1(f)). The top electrode (region B) is surrounded by a buried floating n-doped guard ring (region D) to screen against excess leakage current from surface, interface, and bulk defect states from the surrounding region [24]. Two detector models are studied in this work: a previous generation incorporating four circular CS, each with 20 µm diameter and having a 5.9 nm-thick gate oxide ("Type I", Fig. 1(d)); and a new generation utilising a single CS of 60 µm edge length ("Type II", Fig. 1(e)) with either a 5.2 nm or 3.2 nm-thick gate oxide. Full details on the general detector design and fabrication process are described elsewhere [14]. Key properties of the specific detectors employed in this work are summarised in Table I.

Each ion impact event is measured using the ion beam induced charge (IBIC) technique [25]. As each ion strikes the detector, a cascade of electron-hole (e-h) pairs is created along its deceleration trajectory. The number of e-h pairs produced in the sensitive silicon detection volume n_0 is proportional to the remaining kinetic ion energy after passing through the oxide passivation "dead" layer $E' = E - \delta E$ and is made up of contributions from the primary ion as well as those of respective recoiled target atoms. Through a process of diffusion and drift (from the internal electric field or with an additional external reverse bias), the e-h pairs become separated. A fraction may recombine at trapping sites in the silicon bulk as well as at the Si-SiO$_2$ interface, resulting in $n < n_0$ e-h pairs reaching the electrodes. By connecting the detector to a charge-sensitive preamplifier circuit, the electrical impulse due to ion-induced charge movement towards the electrodes can be measured. The detector's ion detection ability is typically quantified by the charge collection efficiency $\eta = n/n_0$.

In this work, an ultra-low noise preamplifier based on the design of Bertuccio et al. [26] is employed. It incorporates a forward-biased junction field effect transistor (JFET) [27] which, together with the detector, is mounted on an integrated thermoelectric cooling element (see Fig. 1(b)). The
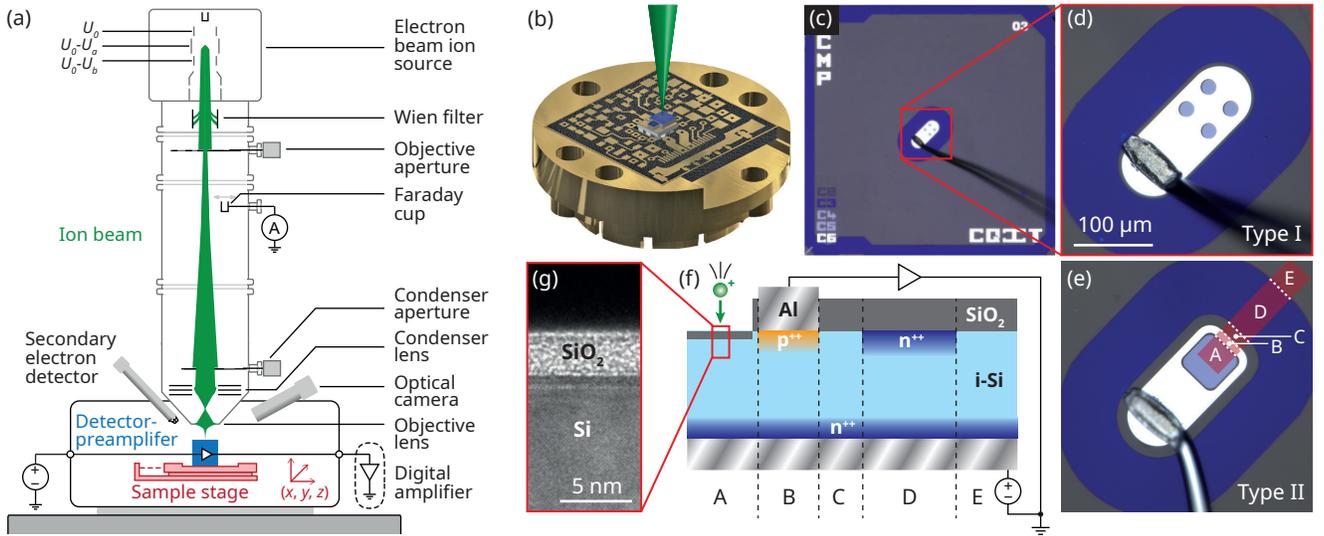
FIG. 1. (a) Schematic of the FIB machine, equipped with an electron-beam-ion-source and integrated single ion detector electronics mounted on a precision sample stage. The ion beam profile is based on an actual ray tracing simulation [21]. (b) Computer-aided design image of the single ion detector setup. It consists of a preamplifier circuit board housed in a metal case of 4 cm diameter. The ion beam (green) is focused onto an on-chip silicon p–i–n diode detector that is directly connected to a low noise junction field effect transistor (JFET). Both the detector and the JFET are mounted on a thermoelectric cooling element at the centre of the board. (c) Optical micrograph showing the top-view layout of the ion detector diode. Two different layouts of (d) $4 \times 20 \, \mu m$-diameter construction sites (CS) or (e) one central $60 \times 60 \, \mu m^2$ CS are available. (f) Cross-sectional schematic of the detector (as indicated in (e)) showing the sandwich-type p–i–n diode structure. The gate oxide inside the CS is between $3 - 6$ nm thick, whilst the surrounding field oxide exhibits ~ 65 nm thickness. The aluminium electrodes are approximately 200 nm thick. (g) Representative cross-sectional transmission electron microscope image of the CS of a detector.

TABLE I. Summary of the individual properties of each detector used in this work

Detector name	Wafer ID	Gate oxide thickness (nm)	Field oxide thickness (nm)	CS type
A-1	A	5.2[a]	62	II
B-1	B	5.9	65	I
C-1	C	3.2	68	II
C-2	C	3.2	68	II

[a] An additional 500 nm thick layer of SU-8 resist was deposited on the gate oxide and formed into a calibration pattern via electron beam lithography.

detector is operated under reverse bias by applying +10 V to the lower electrode and connecting the top electrode to the JFET gate via a wire bond. Further signal processing occurs entirely within the integrated preamplifier. Modest cooling to $-10 \, °C$ is applied during operation, resulting in a typical root-mean-square (r.m.s.) noise of ~ 70 eV [14]. The pre-amplified signal output is then fed into an Amptek PX5 digital pulse processor [28] which performs trapezoidal pulse shaping ($\tau = 9.6 \, \mu s$ peaking time), amplification, and digitisation. Channel-to-energy conversion is accomplished by comparing the ion response against that of a ^{57}Co calibration radionuclide that emits characteristic Fe 6.40 keV K_α and 7.06 keV K_β X-ray photons. The correlation between the known ion beam position (provided directly from the FIB pattern generator) and the detected signal from each ion impact is realised using a custom-written NI LabVIEW program.

III. RESULTS AND DISCUSSION

A. Setup Characterisation

1. FIB Performance

Evaluation of the ion beam profile took place with detector A-1, where an additional 500 nm of SU-8 resist was deposited on the surface and selectively developed into a calibration pattern using electron beam lithography. A checkerboard layout with pitch size ranging from $4 - 0.5 \, \mu m$ was formed inside the CS, as shown in Fig. 2(a). The detector was subsequently placed inside the FIB machine, where a 6 keV $^1H_2^+$ beam was then scanned over a $10 \times 10 \, \mu m^2$ area inside the CS. Light ions are employed for the initial characterisation because they produce less sample damage and greater ionisation than heavier species for the same kinetic energy [20]. Each $^1H_2^+$ molecule ion dissociates quasi-instantaneously upon surface impact, due to the energy transfer exceeding the binding energy by several orders of magnitude [29]. The constituent ions share the total kinetic energy in equal parts (3 keV per H^+) and decelerate simultaneously inside the detector. Ions that strike areas protected by the resist cannot produce signal pulses, as its thickness is large enough to prevent incident ions from entering the sensitive detector volume [30]. In resist-free areas, the average penetration depth is ~ 47 nm below the Si-SiO_2 interface, and a combined sum of 1560 e-h pairs (subject to Poisson statistics) is produced per H_2^+ ion [30]. The shallow implantation depth compared to the overall detector thickness

(a)

SiO$_2$

Resist

2 µm

(b)

y
x

(c)

[Figure 2(c) plot: Intensity (arb. units) vs Distance (µm), y-axis 0 to 20, x-axis 0 to 12]
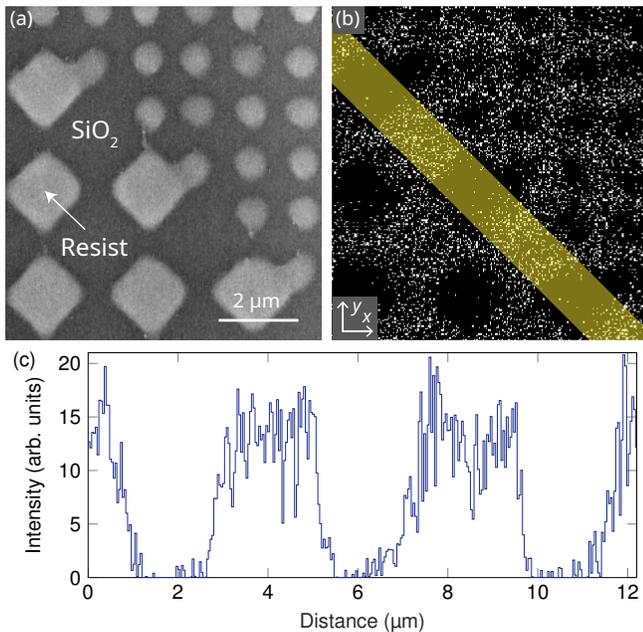
Intensity (arb. units)

Distance (µm)

FIG. 2. (a) Secondary electron image taken inside the construction site of detector A-1, showing the checkerboard pattern formed by a 500 nm thick SU-8 resist layer deposited on the gate oxide. Squares of 2 µm and 1 µm pitch can be seen. (b) Corresponding 256×256 pixel spatially-resolved single ion impact event map, created by a focused beam of 6 keV H$_2^+$ ions. A total of 6521 ion impacts were recorded, with each white pixel corresponding to a single detected ion impact event. The ion impact rate was approximately 20 ion/s and the dwell time was fixed at 8 ms. Objective and condenser aperture sizes were set to 1 µm and 10 µm, respectively. (c) Linescan extracted from the yellow-shaded line in (b) and integrated over its width.

causes the IBIC signal pulse to be dominated by electron drift towards the back electrode, whereas holes contribute to only a minor degree [31].

Fig. 2(b) demonstrates a spatially-resolved map of ion-induced signal events captured with optimised FIB column parameters. A comparison against the actual calibration pattern visualised via scanning electron microscopy (Fig. 2(a)) shows that the overall shape appears well-reproduced by the system. The majority of detected ion impact events originate from resist-free areas, and the pattern aspect ratio is preserved, indicating optimised ion beam stigmator settings. However, some residual scattered events are also seen to occur within resist-covered areas. To better understand this finding, intensity line profiles were extracted from the ion impact event map, with an example shown in Fig. 2(c). The left-hand edge of each plateau (with respect to Fig. 2(c)) appears to have a consistently greater spread than the right-hand edge, with this highly directional behaviour indicating unwanted residual FIB coma effects. This can be addressed by further fine adjustment of the ion optical alignment [21]. The beam spot of the system was thus determined by fitting an error function to the unaffected right-hand edge. An average FWHM of (181 ± 14) nm was obtained along an extended edge feature. This is a substantial improvement over other EBIS-based FIB machines,

where values of between $500 - 1000$ nm have been reported [23, 32, 33]. However, this does not represent the lower resolution limit of this system. An even smaller spot size can be obtained by further reducing the FIB aperture size to below 100 nm – ion-induced event maps can be still be generated in a matter of minutes, despite the predicted <1 fA beam current. Custom-fabricated nanoapertures are currently under evaluation for this purpose [34].

2. Ion Energy Measurement & Mapping

To confirm correct operation of the system, a 12 keV ^{1}H$_2^+$ ion beam was scanned over a detector with a previously-measured response to similar energy ^{1}H$_2^+$ ions [14] (detector B-1, Type I) and the signal pulse amplitudes were recorded. In the absence of incident ions, an r.m.s. noise of $\sim$110 eV was measured. This is about 40 eV greater than other detectors from the same wafer [14] and can be attributed to an additional capacitance at the JFET input gate from a second detector that was connected in parallel during this experiment. However, this is sufficient for high confidence low-energy single ion detection, as discussed later. A total of 10,000 single ion impact events were recorded, with the resulting signal pulse spectrum shown in Fig. 3(a). The spectrum is dominated by a broad main peak centred at 2.5 keV, with a fraction of its lower energy side cut off due to the noise discriminator threshold. On the high-energy side, a separate small signal peak occurs at 5.8 keV and approximately 700 eV FWHM. One further isolated small peak, centred at 11.3 keV and approximately 600 eV FWHM, can also be identified.

The corresponding spatially-resolved charge signal pulse map is shown in Fig. 3(b) and reveals the origin of each peak. Each pixel is colour-coded according to the charge collection efficiency η determined from the pulse recorded at the given location. The overall map features agree well with the optical top-view micrograph of the same device shown in Fig. 1(d). As expected, the isolated highest-energy signal peak originates inside the CS array (region A in Fig. 1(f)). Here, the initial ion energy loss from stopping in the thin gate oxide (see Table I) is negligible. The known low defect concentrations found in the silicon bulk and at the thermal gate oxide interface [14, 35] maximises the number of e-h pairs produced in the sensitive volume, resulting in $\eta \approx 1$. For a 12 keV H$_2^+$ molecule ion, $\sim$95% of its kinetic energy is dissipated in electronic stopping by e-h pair generation according to the model of Funsten and Ziegler [30, 36]. With the signal peak centre located at $\sim$11.3 keV, our results are consistent with this model and also with previous experimental results obtained with a collimated beam from a conventional plasma-filament ion source [14], thus confirming the correct functionality of the system. Additional spectra obtained from independently scanning each individual CS are also shown in Fig. 3(c). There appears to be minimal variation in η between each CS, and the absence of isolated events outside the main signal peak indicates negligible artificial influences – e.g. from ion scattering or gate oxide effects such as thickness fluctuations and surface debris.

Outside the CS array, the top metal electrode pad (region B) yields no single ion detection events, agreeing with TRIM simulations that predict 100% of 12 keV H_2^+ molecule ions should stop completely within the metal layer [30]. Next, the narrow undoped region between the top electrode and the n-guard ring (region C) gives rise to the satellite signal peak located at 6 keV. Here, the ions experience increased stopping in the thicker field oxide (see Table I) and lose approximately half of their initial kinetic energy before reaching the sensitive detector volume [30]. Hence, only approximately half the number of e-h pairs is generated in this region, compared to in region A. Further, no signal events are recorded within the n-guard ring area (region D) due to the very high phosphorous doping concentration (3×10^{19} cm^{-3}), representing a volume of very effective e-h pair recombination.

Finally, the outer area (region E) yields the dominant signal peak in Fig. 3(a), with the peak size coming from its relatively large area fraction of the detector. Here, the n-guard ring strongly attenuates the internal reverse bias drift field, rendering the slower charge carrier diffusion process (minority carrier lifetimes typically $\sim$100 ns, compared to ps drift times [37]) as the dominant transport mechanism. The spatially isotropic nature of e-h pair diffusion, combined with lifetime-limiting interface and bulk defects, results in a quick decline of η with growing lateral distance from the n-guard edge. However, we emphasise that ions are not actually designed to be implanted and detected in this region. Instead, the earlier result showing $\eta \rightarrow 1$ within each CS (region A) is the key conclusion to draw from this initial experiment.

B. Defect Measurement and Analysis

Turning to our application to silicon donor-based quantum computing, we now evaluate Type II detectors incorporating a large-area CS needed to host large-scale donor arrays. We will test the key array formation requirement: all implanted ions must be able to be detected with a high degree of confidence at their predefined target locations. More precisely, η must meet two criteria in the CS: (1) the average value must be near-unity, and (2) it must be spatially homogeneous. As previously introduced, the IBIC technique is inherently sensitive to defects located in the bulk [39, 40] and at interfaces [41, 42] that act as trapping/recombination centres for ion-induced free e-h pairs. Especially for criterion (2), local effects such as gate oxide thickness fluctuations or residual nanoscale surface debris can contribute towards increased ion stopping before an ion reaches the sensitive detector volume, leading to highly localised areas of reduced η. This cannot be readily evaluated with broad-beam ion implantation, and instead a scanned focused ion microprobe must be used. Furthermore, low kinetic energy keV ions are needed (unlike in conventional MeV IBIC experiments [20]) to ensure that a similar depth scale to that used for eventual donor array ion implants is probed.

To evaluate the presence of such defects, two representative detectors from the same fabrication wafer (see Fig. 4(a) and (b)) were selected at random and mapped with a scanned 12 keV H_2^+ beam. Fig. 4(c) shows a high-resolution map of
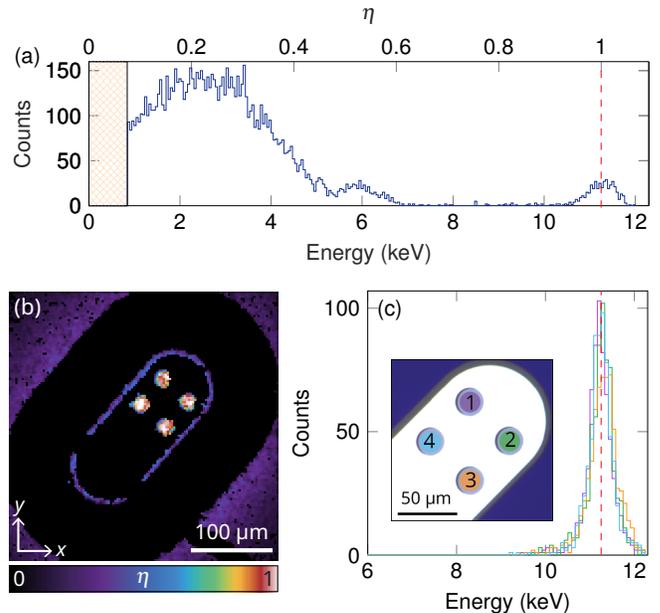

FIG. 3. (a) Signal pulse spectrum of detector B-1 exposed to a scanned 12 keV H_2^+ beam. The three peaks correspond to different regions of the device with varying η, as discussed in the main text. The hatched interval $[0, 0.84]$ keV indicates the noise discriminator regime. The red dashed line indicates an average charge collection efficiency of $\langle \eta \rangle = 1$. (b) Spatially resolved 128×128 pixel map of the data presented in (a). The dark strip extending to the bottom-right corner is due to the shadowing effect of the 20 μm-thick wire bond attached to the metal top electrode. (c) Signal pulse spectra extracted from detailed scans performed inside each construction site (as indicated in each highlighted area in the inset optical image). Each spectrum is comprised of $\sim$650 single ion impact events.

η in detector C-1. The CS exhibits ideal signal characteristics and clearly fulfills both criteria. A linescan taken diagonally along its cross-section (Fig. 4(e)) confirms fluctuations in η of $< 3\%$. These can be attributed to the statistical nature of a multi-atom collision cascade each ion experiences, due to (i) variations in the residual kinetic ion energy after transmitting the gate oxide, (ii) variations in the electronic ion stopping fraction in the sensitive region, and (iii) Fano statistics of e-h pair generation due to electron and hole scattering in the silicon lattice [43]. This is also the origin of the signal peak width visible in Fig. 3(c). The sharp decrease in η at the CS perimeter is due to an abrupt transition between the gate oxide and the thicker surrounding field oxide.

The situation is markedly different for detector C-2. As shown in Fig. 4(d) and (e), three distinct regions of different η are observable within the CS. The right-hand third (region I) exhibits comparably uniform signal characteristics with near-unity η, similar to detector C-1. However, the remaining regions indicate the presence of defects. Two pockets of degraded $\eta < 0.5$ occur at the top and in the centre of the CS (region II). They span approximately 10×20 μm in lateral dimensions. In the left-hand third of the CS (region III), a more uniform spatial detector response is apparent, albeit with a reduced average $\eta \approx 0.9$. To better understand
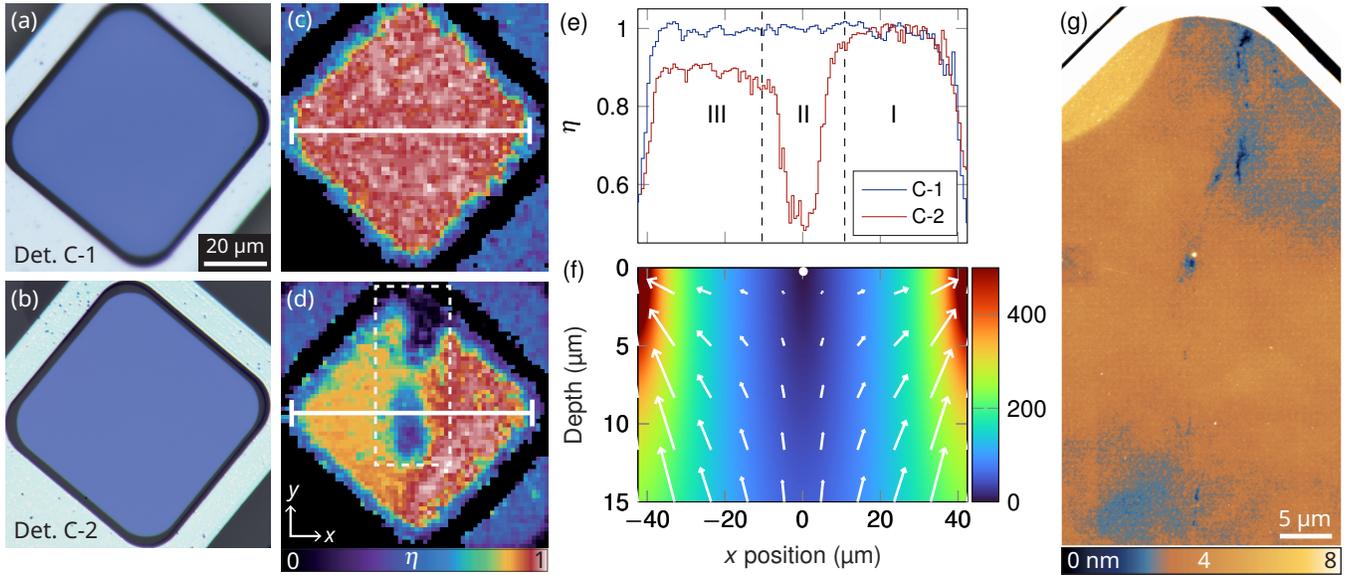
FIG. 4. $100\times$ optical micrographs showing the construction sites of (a) detector C-1 and (b) detector C-2. (c), (d) Corresponding spatially-resolved 256×256 pixel signal pulse maps captured using a scanned 12 keV H_2^+ beam with a ~20 ion/s incidence rate and a fixed 8 ms dwell time. A two-pixel binning algorithm was applied to compensate for some void pixels. (e) Line profiles of η, extracted along the horizontal diagonal (x-axis) of the construction site of each detector (indicated by white lines in (c) and (d)). Regions of similar η for detector C-2 are indicated and discussed in the main text. (f) COMSOL® simulation [38] showing the strength and direction of the internal electric field $\mathbf{E}$ (V cm^{-1}) inside an ideal detector, taken along the same cross-section as in (e). An external reverse bias of -10 V was applied. Peak doping concentrations of 1×10^{16} cm^{-2} were specified in the p and n ohmic contact regions against a 1×10^{11} cm^{-2} n-type background. An interface defect density of $D_{it} = 1 \times 10^{11}$ cm^{-2}eV^{-1} and a fixed oxide charge of $Q_f = 1 \times 10^9$ cm^{-2} were assumed in the gate oxide. The white dot at the image centre indicates the expected average implantation depth of 12 keV H_2^+ ions according to TRIM calculations [30]. (g) Topography map of detector C-2 obtained with atomic force microscopy. The scan area is indicated by the dashed white rectangle in (d).

the charge collection dynamics, a COMSOL® simulation [38] of the electric field $\mathbf{E}$ inside an ideal ($\eta = 1$) detector was run, with the results shown in Fig. 4(f). $\mathbf{E}$ is largely uniform and vertically aligned deep inside the detector, but increasingly re-aligns horizontally in the vicinity of the surface. This is accompanied by a lateral gradient in the absolute field strength, with a near field-free region existing in the centre of the CS to a depth of a few μm. This is many times the ion implantation depth ((88 ± 30) nm [30]), suggesting that in this region, the motion of ion-generated free e-h pairs is initially characterised by diffusion and later becomes dominated by drift transport in the deeper silicon bulk. The conclusion is that a Si crystal with few point/extended defects (see Fig. 1(g)) and a well-passivated surface from a thermally-grown oxide [44] appears sufficient to create an environment with diffusion lengths spanning tens of μm, as exhibited by detector C-1. This is clearly not the case in detector C-2.

The shallow ion probing depth suggests that the physical origin of the defective regions in detector C-2 may be surface-related. Atomic force microscopy was thus performed in the affected area of the CS, as indicated in Fig. 4(d)). The corresponding topography map is shown in Fig. 4(g). A hairline crack extending from the top corner to the centre of the CS can be identified, with lateral dimensions varying between a few hundred nm to a few μm. In some areas, the crack has a depth of up to 4 nm. This is comparable to the thermal gate oxide thickness, suggesting that an error during the fabrica-

tion process (e.g. residual surface debris present during spin coating or a mechanical scratch from wafer handling) resulted in its local etching. The complete removal of a thermally-grown oxide and subsequent exposure of the underlying silicon material leads to the formation of a native oxide (2 − 3 nm thickness), typically characterised by defect interface trap densities $D_{it} > 10^{13}$ cm^{-2}eV^{-1} and fixed oxide charge densities $Q_f > 10^{12}$ cm^{-2} [45]. These values lie several orders of magnitude higher than those measured in a typical thermal gate oxide [35, 46], thus representing a concentrated region of effective e-h pair trapping and recombination. The corresponding signal pulse map (Fig. 4(d)) clearly reflects a reduced charge carrier lifetime in and around this damaged region, where only 20 − 50 % of the ion-induced e-h pairs are collected at the detector electrodes.

The non-uniform ion detection response exhibited by detector C-2 therefore makes this device unsuited to hosting a large-scale donor array, demonstrating the crucial need for a low interface density passivation thermal oxide in donor-based silicon quantum computing applications. However, this appears to be an isolated case, with other detectors from the same wafer also tested (not shown) and confirmed to be fit for purpose. Moreover, these results demonstrate the importance of using application-relevant low energy keV ions in the initial device characterisation, in order to understand and troubleshoot the device behaviour at the near-surface. The versatility of this system should also be pointed out in allowing not

only analysis of silicon-based electronic devices, but potentially those based on other IBIC-compatible platforms, such as SiC, diamond, and III-V materials [20].

C. Mask-Free Deterministic Ion Implantation

We now turn our attention towards reconfiguring the setup to enable future controlled implantation of individual $^{31}P^+$ ions for use in spin-based quantum computing. In these experiments, 24 keV $^{40}Ar^{2+}$ ions (acceleration potential = 12 kV) were employed. Each ion penetrates (28 ± 13) nm below the Si-SiO$_2$ interface and generates an average of $\sim$1700 e–h pairs in the active detection volume [30]. Although the electronic and spin properties of ^{40}Ar do not make it compatible with quantum information processing in silicon, its ion stopping characteristics are very similar to the ^{31}P donor-qubit [48], providing a good estimate of the ion detection signal response and thus allowing a robust assessment of further adapting the FIB setup for this ultimate purpose.

In a large-scale quantum computing device incorporating surface control gates [7, 49], it is important to minimise the depth placement uncertainty (longitudinal straggle) of each donor. Too deep placement results in poor spin-dependent tunnel coupling of the donor electron, whereas too shallow placement causes the donor to be located adjacent to or in the oxide and consequently inactivated. The straggle can be reduced by lowering the implantation energy (see Table II). However, this also reduces the number of ion-induced e-h pairs and thus causes the amplitude of each charge pulse signal to lie near the noise threshold, thereby increasing the likelihood of > 1 donor per implant site. The net result is a reduced ensemble coherence time from uncontrolled nearby donor-donor coupling. The solution is to reach an optimum balance between the placement uncertainty and the ion detection confidence $\Xi(q_{t0})$, defined as the fraction of detected single ion events (counts above the noise discriminator threshold q_{t0}) to the total number of incident ions [14]. To predict $\Xi(q_{t0})$, a $5 \times 5 \, \mu m^2$ area located at the centre of the CS (left inset of Fig. 5) in detector C-1 was continuously scanned with a 24 keV Ar^{2+} beam until 2000 signal events were recorded. The resulting signal pulse spectrum is shown in Fig. 5. Compared to $^1H^+$, the heavier mass of $^{40}Ar^{2+}$ results in only 25 % of the initial ion kinetic energy being dissipated into electronic stopping [36], shifting the peak centroid down to $\sim$6.1 keV. The peak also appears broader due to a greater statistical variation in the fraction of electronic energy loss of each ion. Nevertheless, a clear interval between the lowest detected count (at 2.5 keV) and the noise discrimination threshold (at 0.64 keV) lacking any signal events is seen, strongly suggesting that 100% of the incident ions were successfully detected.

A robust assessment of $\Xi(q_{t0})$ is done by comparing the experimentally obtained signal pulse spectrum with that generated by a Crystal-TRIM simulation [47] for an ideal ($\eta = 1$) silicon detector with the same gate oxide thickness. Good agreement between the experimental and simulated spectra is observed, allowing us to extract a detection confidence of $\Xi(q_{t0}) \geq 99.99\%$. The effect of the accumulated ion fluence on the signal pulse spectrum [50] was additionally considered by comparing the first and last 200 detected events, as shown in the right inset of Fig. 5. Within the statistical uncertainty of the two sub-spectra, no evidence of a systematic peak shift or broadening is seen, suggesting that even moderate ion-induced crystal damage (an average Ar^{2+} inter-ion spacing of 112 nm – almost 4x the intended donor density for the chosen quantum device architecture [7]) does not lead to a significant degradation in η.

Compared to previous detector generations incorporating a standard 6 – 8 nm gate oxide [14], detector C-1 features an ultra-thin 3.2 nm gate oxide (see Fig. 1(g)) from optimisation of the oxide growth process. Similar CMOS devices incorporating sub-5 nm gate oxides have been shown to be susceptible to elevated defect concentrations [51]. However, the near-unity η value obtained here suggests that the density of interface defect traps and fixed oxide charge within this ultra-thin gate oxide is in fact comparable to that measured in previous-generation devices [8, 10]. A thin gate oxide also provides an improved controlled silicon doping yield Y_{dop}, defined as the fraction of detectable single ion impacts where the primary dopant ion also entirely transmits the gate oxide to stop inside the silicon crystal. Events where the primary ion stops inside the oxide may still produce a detectable signal, because forward-recoiled Si and O atoms from the oxide can also contribute to an overall charge signal pulse event. These events appear to be extremely rare for this detector generation, with Crystal-TRIM simulations [47] predicting $Y_{dop} = 99.95\%$ for 24 keV Ar^{2+} ions. Using a Type-I detector, we previously reported a single ion detection confidence of $\Xi(q_{t0}) = 99.85\%$ for 14 keV $^{31}P^+$ ions, but the actual doping yield was limited to $Y_{dop} = 98.1\%$, due to 1.9% of the incident $^{31}P^+$ ions stopping inside the 6 nm gate oxide [14]. Extrapolating the present results obtained with Ar ions, we expect a factor 5 enhancement to $Y_{dop} = 99.62\%$ for 14 keV $^{31}P^+$ ions when implanted into the Type-II detector, comfortably exceeding the latest estimates of tolerable donor qubit loss fault thresholds (90 – 95 %) [52]. The production of $^{31}P^+$ ions from an EBIS has already been demonstrated [53], and is currently forthcoming in our setup.

The lateral placement accuracy of each implanted ion is the additional component in determining our setup's suitability for scalable donor array fabrication in silicon, and can be split into two independent scattering processes. First, the uncertainty of each ion's lateral impact point on the detector surface comes from the fixed spot size of the FIB. Second, lateral ion straggling takes place inside the target material (see Table II) as a direct result of the random collision cascade each ion makes with target atoms upon stopping. Although the present 181 nm (FWHM) spot size is not compatible with the sub-50 nm lateral donor placement constraints of the flip-flop qubit architecture [7], we expect a further spot size reduction to <30 nm to be realistically achievable by employing custom-fabricated 100 nm diameter lens apertures [34], as mentioned earlier. In this regime, effects from the spot size and the lateral ion straggling in silicon should contribute more or less equally to the overall ion placement precision. Furthermore, the expected reduction in beam current from the smaller aperture

TABLE II. Properties of selected ion species (and in some cases, varied kinetic energies) when implanted through a 3.2 nm-thick SiO_2 layer into (100) Si, as modelled by Crystal-TRIM [47]. The implantation depth is calculated from the Si-SiO_2 interface. The number of e-h pairs is calculated in the sensitive detection volume, with a 640 eV noise floor assumed to determine the ion detection confidence. Starred entries (*) denote results that have not yet been experimentally verified.

Species	E_{kin} (keV)	Implantation depth $\pm$ straggle (nm)	Lateral straggle (nm)	n_0 (e-h pairs)	$\Xi(q_{t0})$ (%)	Y_{dop} (%)
$^1H_2^+$	12	86.9 ± 31.2	40.3	3112	≥ 99.99	99.91
$^{40}Ar^{3+}$	36	40.3 ± 17.6	14.4	2764	≥ 99.99	99.99
$^{40}Ar^{2+}$	24	27.8 ± 13.0	10.6	1695	≥ 99.99	99.95
$^{40}Ar^+$	12	14.6 ± 7.8	6.3	625	99.84	99.68
$^{31}P^+$	14	19.7 ± 10.7	9	1108	99.98*	99.62*
$^{31}P^+$	9	12.9 ± 7.7	6.5	643	99.85*	98.98*

size can be offset by the highly adjustable nature of the EBIS emission intensity, yielding a similar expected on-target implantation rate to that used in the present experiments. Precision localisation of single ions has already been demonstrated with a masked approach, where a nanoaperture was milled in the tip of an atomic force microscope cantilever and placed directly above the sample to collimate the beam [54]. However, adapting this technique below the 30 nm level may be technically challenging due to expected lateral and axial ion straggling effects from the aperture. Particularly for high aspect ratio nanoapertures, an unacceptably large proportion of ions can be implanted hundreds of nm away from their intended target locations [55]. This effect can also be aggravated by the accumulated ion fluence seen by the cantilever, whereby the nanoaperture can shrink and eventually completely close over time [54, 56]. The use of a mask-less, focused implantation method, such as the FIB system employed in this work, may present a viable avenue around this.

Our system also has the advantage that highly charged ions (up to completely ionised) can readily be supplied by the EBIS. Especially for heavy donors such as ^{123}Sb and ^{209}Bi, the additional potential energy deposited by these ions in the detector [57] may result in an increased $\Xi(q_{t0})$. Alongside recent studies from systems that detect single in-flight ions just prior to the implantation event [58, 59], our results represent a pathway towards the scalable engineering of near-surface donor qubit arrays with nanoscale placement precision.

FIG. 5. Signal pulse spectrum of detector C-1 irradiated with a focused beam of 2,000 24 keV Ar^{2+} ions, raster-scanned over a 5×5 μm^2 area inside the construction site (as indicated in the left inset; scale bar = 20 μm). The dwell time was set to 1 ms and the incidence rate was $\sim$10 ion/s. The low level discriminator was set to 640 eV, corresponding to the hatched region. Also shown are the results of normalised Crystal-TRIM simulations [47] of the same experiment, performed with 20,000 ions. Right inset: sub-spectra from the first and last 200 recorded counts.

IV. CONCLUSION

We have introduced an electronic device characterisation system that uses a FIB equipped with an electron-beam-ion-source as well as ultra-low noise single ion detection technology to enable deterministic control over the number and position of implanted ions. The highly adjustable source can produce ions with energies between $3 - 300$ keV, implanted at rates between $0.1 - 100$ ion/s, focused down to a spot size of 180 nm (FWHM). Through the ion beam induced charge principle, we use silicon p–i–n diode detectors to measure electron-hole pairs generated by each ion impact event and correlate this with the beam position. Using an updated generation of ion detectors featuring an enlarged 60×60 μm^2 sensitive area and an ultra-thin 3.2 nm gate oxide, we first spatially map the internal electric field to within 100 nm of the surface using 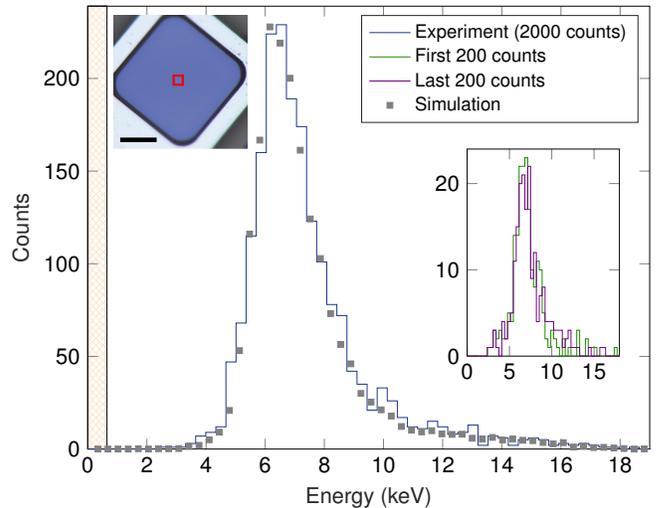a rastered 12 keV $^1H_2^+$ ion probe. The results highlight the destructive effect that localised regions of defect-rich native oxide play in suppressing the detection response, whereby >50% of the initially diffused charge can be lost to associated interface states. Nevertheless, near-unity charge collection efficiency is measured in the sensitive area of functional detectors, thus confirming our devices are fit for purpose. Next, we modify the system to perform counted implantation of 2000 $^{40}Ar^{2+}$ ions at 24 keV into a pre-defined 5×5 μm^2 area, obtaining $\geq 99.99\%$ single ion detection confidence. This approach foregoes the need for a mechanical implant mask that may introduce additional ion scattering. With an upcoming system upgrade to incorporate a $^{31}P^+$ ion source and yield a sub-30 nm FIB spot size, we aim to establish a viable method to fabricate large-scale near-surface ^{31}P donor arrays in silicon for multi-qubit entanglement studies.

V. ACKNOWLEDGEMENTS

[1] S. M. Sze, *Semiconductor Devices: Physics and Technology*, 3rd ed. (John Wiley & Sons, 2012).

[2] W. D. Rau, P. Schwander, F. H. Baumann, W. Höppner, and A. Ourmazd, Two-dimensional mapping of the electrostatic potential in transistors by electron holography, Physical Review Letters **82**, 2614 (1999).

[3] IEEE, International Roadmap for Devices and Systems (2021).

[4] A. Asenov, S. Kaya, and J. H. Davies, Intrinsic threshold voltage fluctuations in decanano MOSFETs due to local oxide thickness variations, IEEE Transactions on Electron Devices **49**, 112 (2002).

[5] A. Asenov, A. R. Brown, J. H. Davies, S. Kaya, and G. Slavcheva, Simulation of intrinsic parameter fluctuations in decananometer and nanometer-scale MOSFETs, IEEE Transactions on Electron Devices **50**, 1837 (2003).

[6] B. E. Kane, A silicon-based nuclear spin quantum computer, Nature **393**, 133 (1998).

[7] G. Tosi, F. A. Mohiyaddin, V. Schmitt, S. Tenberg, R. Rahman, G. Klimeck, and A. Morello, Silicon quantum processor with robust long-distance qubit couplings, Nature Communications **8**, 450 (2017).

[8] J. T. Muhonen, J. P. Dehollain, A. Laucht, F. E. Hudson, R. Kalra, T. Sekiguchi, K. M. Itoh, D. N. Jamieson, J. C. McCallum, A. S. Dzurak, and A. Morello, Storing quantum information for 30 seconds in a nanoelectronic device, Nature Nanotechnology **9**, 986 (2014).

[9] J. P. Dehollain, J. T. Muhonen, R. Blume-Kohout, K. M. Rudinger, J. K. Gamble, E. Nielsen, A. Laucht, S. Simmons, R. Kalra, A. S. Dzurak, and A. Morello, Optimization of a solid-state electron spin qubit using gate set tomography, New Journal of Physics **18**, 103018 (2016).

[10] M. T. Mądzik, S. Asaad, A. Youssry, B. Joecker, K. M. Rudinger, E. Nielsen, K. C. Young, T. J. Proctor, A. D. Baczewski, A. Laucht, V. Schmitt, F. E. Hudson, K. M. Itoh, A. M. Jakob, B. C. Johnson, D. N. Jamieson, A. S. Dzurak, C. Ferrie, R. Blume-Kohout, and A. Morello, Precision tomography of a three-qubit donor quantum processor in silicon, Nature **601**, 348 (2022).

[11] J. A. Ivie, Q. Campbell, J. C. Koepke, M. I. Brickson, P. A. Schultz, R. P. Muller, A. M. Mounce, D. R. Ward, M. S. Carroll, E. Bussmann, A. D. Baczewski, and S. Misra, Impact of Incorporation Kinetics on Device Fabrication with Atomic Precision, Physical Review Applied **16**, 054037 (2021).

[12] L. Fricke, S. J. Hile, L. Kranz, Y. Chung, Y. He, P. Pakkiam, M. G. House, J. G. Keizer, and M. Y. Simmons, Coherent control of a donor-molecule electron spin qubit in silicon, Nature Communications **12**, 3323 (2021).

[13] J. M. Poate and K. Saadatmand, Ion beam technologies in the semiconductor world (plenary), Review of Scientific Instruments **73**, 868 (2002).

[14] A. M. Jakob, S. G. Robson, V. Schmitt, V. Mourik, M. Posselt, D. Spemann, B. C. Johnson, H. R. Firgau, E. Mayes, J. C. McCallum, A. Morello, and D. N. Jamieson, Deterministic Shallow Dopant Implantation in Silicon with Detection Confidence Upper-Bound to 99.85% by Ion–Solid Interactions, Advanced Materials **34**, 2103235 (2022).

[15] J. Orloff, High-resolution focused ion beams, Review of Scientific Instruments **64**, 1105 (1993).

[16] P. Li, S. Chen, H. Dai, Z. Yang, Z. Chen, Y. Wang, Y. Chen, W. Peng, W. Shan, and H. Duan, Recent advances in focused ion beam nanofabrication for nanostructures and devices: fundamentals and applications, Nanoscale **13**, 1529 (2021).

[17] N. Klingner, G. Hlawacek, P. Mazarov, W. Pilz, F. Meyer, and L. Bischoff, Imaging and milling resolution of light ion beams from helium ion microscopy and FIBs driven by liquid metal alloy ion sources, Beilstein Journal of Nanotechnology **11**, 1742 (2020).

[18] M. Manoccio, M. Esposito, A. Passaseo, M. Cuscunà, and V. Tasco, Focused Ion Beam Processing for 3D Chiral Photonics Nanostructures, Micromachines **12**, 6 (2020).

[19] P. J. Moll, Focused Ion Beam Microstructuring of Quantum Matter, Annual Review of Condensed Matter Physics **9**, 147 (2018).

[20] E. Vittone, Semiconductor Characterization by Scanning Ion Beam Induced Charge (IBIC) Microscopy, ISRN Materials Science **2013**, 1 (2013).

[21] P. Räcke, R. Wunderlich, J. W. Gerlach, J. Meijer, and D. Spemann, Nanoscale ion implantation using focussed highly charged ions, New Journal of Physics **22**, 083028 (2020).

[22] M. Schmidt, H. Peng, G. Zschornack, and S. Sykora, A compact electron beam ion source with integrated Wien filter providing mass and charge state separated beams of highly charged ions, Review of Scientific Instruments **80**, 063301 (2009).

[23] F. Ullmann, F. Großmann, V. P. Ovsyannikov, J. Gierak, and G. Zschornack, Production of a helium beam in a focused ion beam machine using an electron beam ion trap, Applied Physics Letters **90**, 083112 (2007).

[24] L. Evensen, A. Hanneborg, B. S. Avset, and M. Nese, Guard ring design for high voltage operation of silicon detectors, Nuclear Instruments and Methods in Physics Research Section A: Accelerators, Spectrometers, Detectors and Associated Equipment **337**, 44 (1993).

[25] M. B. Breese, E. Vittone, G. Vizkelethy, and P. J. Sellin, A review of ion beam induced charge microscopy, Nuclear Instruments and Methods in Physics Research, Section B: Beam Interactions with Materials and Atoms **264**, 345 (2007).

[26] G. Bertuccio and A. Pullia, Room temperature X-ray spectroscopy with a silicon diode detector and an ultra low noise preamplifier, IEEE transactions on nuclear science **41**, 1704 (1994).

[27] Moxtek Inc., N-Channel Ultra-low Noise JFETs Catalog (2004).

[28] Amptek Inc., A250 Charge Sensitive Preamplifer Datasheet (2017).

[29] R. Cooks, T. Ast, and M. Mabud, Collisions of polyatomic ions with surfaces, International Journal of Mass Spectrometry and Ion Processes **100**, 209 (1990).

[30] J. F. Ziegler, M. D. Ziegler, and J. P. Biersack, SRIM - The stopping and range of ions in matter (2010), Nuclear Instruments and Methods in Physics Research, Section B: Beam Interactions with Materials and Atoms **268**, 1818 (2010).

[31] E. Vittone, Z. Pastuovic, P. Olivero, C. Manfredotti, M. Jaksic, A. Lo Giudice, F. Fizzotti, and E. Colombo, Semiconductor characterization by scanning ion beam induced charge (IBIC) microscopy, Nuclear Instruments and Methods in Physics Research, Section B: Beam Interactions with Materials and Atoms **266**, 1312 (2008).

[32] S. Guillous, C. Bourin, B. Ban D'Etat, A. Benyagoub, A. Cassimi, C. Feierstein, E. Gardés, E. Giglio, S. Girard, C. Grygiel, A. Houel, H. Lebius, A. Méry, I. Monnet, J.-M. Ramillon, J. Rangama, F. Ropars, E. Verzeroli, M. Viteau, and A. Delobbe, A new setup for localized implantation and live-characterization of keV energy multiply charged ions at the nanoscale, Review of Scientific Instruments **87**, 113901 (2016).

[33] M. Schmidt, P.-F. Laux, J. Gierak, and G. Zschornack, EBIS-based HCI micro-beams, in *AIP Conference Proceedings*, Vol. 2011 (2018) p. 090027.

[34] D. Emmrich, A. Beyer, A. Nadzeyka, S. Bauerdick, J. C. Meyer, J. Kotakoski, and A. Gölzhäuser, Nanopore fabrication and characterization by helium ion microscopy, Applied Physics Letters **108**, 163103 (2016).

[35] B. Johnson, J. McCallum, L. Willems van Beveren, and E. Gauja, Deep level transient spectroscopy study for the development of ion-implanted silicon field-effect transistors for spin-dependent transport, Thin Solid Films **518**, 2524 (2010).

[36] H. Funsten, S. Ritzau, R. Harper, and R. Korde, Response of 100% internal carrier collection efficiency silicon photodiodes to low-energy ions, IEEE Transactions on Nuclear Science **48**, 1785 (2001).

[37] M. B. Breese, A theory of ion beam induced charge collection, Journal of Applied Physics **74**, 3789 (1993).

[38] COMSOL AB, COMSOL Multiphysics® v5.6 (2020).

[39] E. C. Auden, J. L. Pacheco, E. Bielejec, G. Vizkelethy, J. B. Abraham, and B. L. Doyle, Sub-Micron Resolution of Localized Ion Beam Induced Charge Reduction in Silicon Detectors Damaged by Heavy Ions, IEEE Transactions on Nuclear Science **62**, 2919 (2015).

[40] E. Vittone, Z. Pastuovic, M. B. Breese, J. Garcia Lopez, M. Jaksic, J. Raisanen, R. Siegele, A. Simon, and G. Vizkelethy, Charge collection efficiency degradation induced by MeV ions in semiconductor devices: Model and experiment, Nuclear Instruments and Methods in Physics Research, Section B: Beam Interactions with Materials and Atoms **372**, 128 (2016).

[41] G. Vizkelethy, D. K. Brice, and B. L. Doyle, Heavy ion beam induced current/charge (IBIC) through insulating oxides, Nuclear Instruments and Methods in Physics Research Section B: Beam Interactions with Materials and Atoms **249**, 204 (2006).

[42] A. M. Tonigan, D. Ball, G. Vizkelethy, J. Black, D. Black, J. Trippe, E. Bielejec, M. L. Alles, R. Reed, and R. D. Schrimpf, Impact of Surface Recombination on Single-Event Charge Collection in an SOI Technology, IEEE Transactions on Nuclear Science **68**, 305 (2021).

[43] E. Steinbauer, P. Bauer, M. Geretschläger, G. Bortels, J. Biersack, and P. Burger, Energy resolution of silicon detectors: approaching the physical limit, Nuclear Instruments and Methods in Physics Research Section B: Beam Interactions with Materials and Atoms **85**, 642 (1994).

[44] D. M. Fleetwood, P. S. Winokur, R. A. Reber, T. L. Meisenheimer, J. R. Schwank, M. R. Shaneyfelt, and L. C. Riewe, Effects of oxide traps, interface traps, and "border traps" on metal-oxide-semiconductor devices, Journal of Applied Physics **73**, 5058 (1993).

[45] T. Hori, *Gate Dielectrics and MOS ULSIs*, 1st ed. (Springer-Verlag Berlin Heidelberg, Berlin, 1997) pp. 1–352.

[46] J. J. Pla, K. Y. Tan, J. P. Dehollain, W. H. Lim, J. J. L. Morton, D. N. Jamieson, A. S. Dzurak, and A. Morello, A single-atom electron spin qubit in silicon, Nature **489**, 541 (2012).

[47] M. Posselt and J. Biersack, Computer simulation of ion implantation into crystalline targets, Nuclear Instruments and Methods in Physics Research Section B: Beam Interactions with Materials and Atoms **64**, 706 (1992).

[48] T. Hopf, C. Yang, S. E. Andresen, and D. N. Jamieson, The response of silicon detectors to low-energy ion implantation, Journal of Physics: Condensed Matter **20**, 415205 (2008).

[49] C. D. Hill, E. Peretz, S. J. Hile, M. G. House, M. Fuechsle, S. Rogge, M. Y. Simmons, and L. C. L. Hollenberg, A surface code quantum computer in silicon, Science Advances **1**, e1500707 (2015).

[50] A. Simon, G. Kalinka, M. Jaksic, Z. Pastuovic, M. Novak, and A. Kiss, Investigation of radiation damage in a Si PIN photodiode for particle detection, Nuclear Instruments and Methods in Physics Research Section B: Beam Interactions with Materials and Atoms **260**, 304 (2007).

[51] J. H. Stathis and D. J. DiMaria, Reliability projection for ultra-thin oxides at low voltage, in *Technical Digest - International Electron Devices Meeting* (IEEE, 1998) pp. 167–170.

[52] S. Nagayama, A. G. Fowler, D. Horsman, S. J. Devitt, and R. V. Meter, Surface code error correction on a defective lattice, New Journal of Physics **19**, 023050 (2017).

[53] U. Kentsch, S. Landgraf, M. Schmidt, H. Tyrroff, G. Zschornack, F. Grossmann, V. P. Ovsyannikov, and F. Ullmann, Slow highly charged ions for nanoscale surface modifications, Nuclear Instruments and Methods in Physics Research, Section B: Beam Interactions with Materials and Atoms **216**, 196 (2004).

[54] S. Pezzagna, D. Wildanger, P. Mazarov, A. D. Wieck, Y. Sarov, I. Rangelow, B. Naydenov, F. Jelezko, S. W. Hell, and J. Meijer, Nanoscale Engineering and Optical Addressing of Single Spins in Diamond, Small **6**, 2117 (2010).

[55] N. Raatz, C. Scheuner, S. Pezzagna, and J. Meijer, Investigation of Ion Channeling and Scattering for Single-Ion Implantation with High Spatial Resolution, physica status solidi (a) **216**,

1900528 (2019).

[56] J. Li, D. Stein, C. McMullan, D. Branton, M. J. Aziz, and J. A. Golovchenko, Ion-beam sculpting at nanometre length scales, Nature **412**, 166 (2001).

[57] T. Schenkel, A. V. Barnes, T. R. Niedermayr, M. Hattass, M. W. Newman, G. A. Machicoane, J. W. Mc Donald, A. V. Hamza, and D. H. Schneider, Deposition of potential energy in solids by slow, highly charged ions, Physical Review Letters **83**, 4273

(1999).

[58] P. Räcke, D. Spemann, J. W. Gerlach, B. Rauschenbach, and J. Meijer, Detection of small bunches of ions using image charges, Scientific Reports **8**, 9781 (2018).

[59] C. Lopez, A. Trimeche, D. Comparat, and Y. Picard, Real-Time Trajectory Control of Deterministically Produced Ions, Physical Review Applied **11**, 064049 (2019).